Journal of Materials Chemistry A

ROYAL SOCIETY OF CHEMISTRY

PAPER

View Article Online
View Journal | View Issue

Cite this: J. Mater. Chem. A, 2023, 11, 18953

Covalent conjugation of a 'hydroxide-philic' functional group achieving 'hydroxide-phobic' TEMPO with superior stability in all-organic aqueous redox flow batteries†

Noh-Uk Seo,‡[ab] Kyungmi Kim,‡[ac] Jeongmin Yeo,‡[d] Seung Jae Kwak,[e] YongJoo Kim,[f] Hyemi Kim,[c] Mi Song Kim,[c] Jeongi Choi,[c] Yoon Seok Jung,[b] Junghyun Chae,*[c] Jinho Chang *[dg] and Jung Hoon Yang *[a]

We show that a covalent conjugation of a 'hydroxide-philic' functional group to a TEMPO moiety is the key to effectively mitigating chemical degradation during charging and discharging, which hinders OH^- access to oxoammonium sites in the intramolecular regime, leading to a stable TEMPO-based aqueous organic redox flow battery (AORFB) with long-term cyclability. Thorough quantitative analysis of the degradation of 4-OH-TEMPO in its fully discharged and charged states was performed under various pH conditions; it was confirmed that the strong interaction between the oxidized form (*i.e.*, $TEMPO^+$) and OH^- is mainly responsible for the molecular decomposition. Based on this analysis, a TEMPO derivative covalently conjugated with a hydroxide-philic functional group was carefully designed and synthesized; in this article, this derivative is denoted as MIMAcO-TEMPO (4-[2-(*N*-methyl imidazolium) acetoxy]-2,2,6,6-tetramethylpiperidine-1-oxyl chloride). The hydroxide-philic MIMAcO functional group intimately attracts OH^- before the neighboring TEMPO moiety is exposed to OH^- attack. Once an OH^- is combined with the MIMAcO functional group to form the [$(OH^- \rightarrow$ MIMAcO)-$TEMPO^+$] adduct, the oxoammonium site acquires a high electrostatic resistance to OH^-. The change in the sequential binding energy of OH^- to the MIMAcO functional group and the TEMPO moiety was elucidated by density functional theory (DFT) simulations. The estimated resilient characteristics of the oxoammonium site in MIMAcO-$TEMPO^+$ against OH^- and the resultant structural stability were confirmed by UV-vis, NMR, mass spectroscopy, and electrochemical analyses. In AORFB application, MIMAcO-TEMPO showed a remarkable improvement in the capacity decay rate (0.012% per cycle) over 1000 cycles of the galvanostatic charge–discharge test, indicating that this is one of the most stable TEMPO derivatives. In addition, based on the highly hydrophilic properties of the MIMAcO functional group, a high-concentration AORFB was successfully demonstrated with 2.5 M MIMAcO-TEMPO, delivering a record-breaking discharge capacity of 57.1 Ah L^{-1}.

Received 9th June 2023
Accepted 10th August 2023

DOI: 10.1039/d3ta03420h

rsc.li/materials-a

Introduction

In the global transition to renewable energy networks, the role of energy storage systems (ESSs) to efficiently manage energy supply and demand is more than ever in the spotlight.[1–3] Lithium ion batteries (LIBs) have been extensively applied to grid-scale ESSs, but their frequent explosions raise important safety issues.[4,5] As a promising alternative, aqueous redox flow batteries (RFBs) have received considerable attention because of their intrinsic non-flammability and excellent scalability with decoupled power and energy capacities.[6–11] However, all-vanadium RFBs (VRFBs), which are in the demonstration stage, still suffer from high electrolyte cost.[10] Batteries based on inorganic redox active species such as LIBs and VRFBs will

[a]Korea Institute of Energy Research (KIER), Daejeon 34129, Republic of Korea. E-mail: enviroma@kier.re.kr

[b]Department of Chemical and Biomolecular Engineering, Yonsei University, Seoul 03722, Republic of Korea

[c]Department of Chemistry, Sungshin Women's University, Seoul 01133, Republic of Korea. E-mail: jchae@sungshin.ac.kr

[d]Department of Chemistry and Research Institute for Convergence of Basic Science, Hanyang University, Seoul 04763, Republic of Korea. E-mail: jhcechem@hanyang.ac.kr

[e]School of Chemical and Biological Engineering, Institute of Chemical Processes, Seoul National University, Seoul 08826, Republic of Korea

[f]School of Advanced Materials Engineering, Kookmin University, Seoul 02707, Republic of Korea

[g]Department of HY-KIST Bio-convergence, Hanyang University, Seoul 04763, Republic of Korea

† Electronic supplementary information (ESI) available. See DOI: https://doi.org/10.1039/d3ta03420h

‡ These authors equally contributed to this study.

always be subject to resource limitations and thus incur high costs. Recent extensive efforts have targeted aqueous organic RFBs (AORFBs), which utilize organic electroactive molecules in aqueous electrolytes.[12] AORFBs are considered next-generation batteries because of their advantages of natural abundance, potential cost-effectiveness, tunable electrochemical properties, and safety features.

Much progress has been made in the design of water-soluble organic electroactive molecules which constitute anolytes and catholytes for AORFBs. Various organic structures have been explored as anolyte candidates, including alloxazines,[13] quinones,[14–16] viologens,[17–19] and fluorenones.[20] On the other hand, a few organic molecules such as (2,2,6,6,-tetramethyl piperidin-1-yl)oxyl (TEMPO)[19,21–23] and ferrocene[24,25] derivatives are available for use as cathodic redox species. Among them, TEMPO derivatives are the most attractive because they exhibit high redox potential and moderate solubility. TEMPO derivatives contain cyclic nitroxide, in which the free nitroxyl radical acts as an active redox site with a high redox potential of 0.8–1.0 V (*vs.* SHE). Depending on the neighboring functional groups, most TEMPO derivatives are characterized by moderate solubility in water. For example, 4-OH-TEMPO shows a solubility of 2.1 M in pure water.[19]

The nitroxyl radical is sterically protected by the four methyl groups on α-carbons, which enhance its molecular stability; the $TEMPO^{\bullet}/TEMPO^{+}$ redox reaction is known to be redox-reversible within conventional electroanalytical time scales.[26,27] Nevertheless, when using 4-OH-TEMPO as the cathodic active species, significant capacity degradation has been observed.[19,21] Several possible side reactions have been suggested as deactivation mechanisms of TEMPO derivatives. Under acidic conditions, the nitroxyl radical ($R_2N–O^{\bullet}$) may experience disproportionation with H^+, which produces oxoammonium ($R_2N{=}O^+$) and hydroxylamine (R_2NOH),[28,29] among which the latter eventually loses its redox activity due to further degradation into electro-inactive species, such as ring-opened structures.[30,31] Under neutral or alkaline conditions, $TEMPO^+$ in the charged state may chemically react with OH^- and change back to $TEMPO^{\bullet}$ in the discharged state, producing hydroxyl radicals ($OH^{\bullet}$), which are extremely unstable and may further decompose TEMPO into irreversible redox forms. Also, as seen in most other radical reactions, dimerization is a possible TEMPO deactivation mechanism. The intermolecular dimerization reaction has been plausibly suggested to explain concentration-dependent deactivation.[28] However, due to insufficient understanding of the degradation products and conditions, the degradation mechanism of TEMPO derivatives remains unclear.

Recent studies on new TEMPO derivatives have reported improvements of chemical stability in charge/discharge cycles of RFBs. The well-established synthetic approach was to introduce either positively or negatively charged functional groups to the TEMPO moiety, which yield intermolecular coulombic repulsion between TEMPO molecules and consequent mitigation of chemical decomposition *via* possible dimerization.[21–23,30,32,33] However, although these approaches were very effective in addressing the intermolecular dimerization reaction, there was an obvious limitation to inhibiting interaction between $R_2N–O^{\bullet}/R_2N{=}O^+$ and H^+/OH^-. Considering that OH^--attack on $R_2N{=}O^+$ of $TEMPO^+$ is the triggering step of its decomposition process, the accessibility and reactivity of OH^- toward $R_2N{=}O^+$ should be carefully reflected in the molecular design. Song *et al.* introduced imidazole and acetylamino groups to TEMPO to delocalize the electron density along the chemical structure, resulting in an alleviation of deactivation of both $R_2N–O^{\bullet}$ and $R_2N{=}O^+$ in discharged and charged forms.[31] However, those researchers focused on the stability of the TEMPO moiety itself, without aiming for specific side reactions with H^+ or OH^-. In this article, by comparing degradation rates in various reaction environments, we elucidate the main possible reaction routes for TEMPO degradation. Furthermore, we demonstrate a new finding that the functional group with 'hydroxide-philic' nature can behave as a potential intramolecular inhibitor against OH^- access to the oxoammonium site of $TEMPO^+$, resulting in suppression of chemical decomposition.

The solubility of TEMPO derivatives can also be effectively enhanced by adaptation of functional groups. For example, the pyrrolidinium group can increase the intrinsic hydrophilic nature of its TEMPO derivative and induce a high aqueous solubility of 3.35 M.[32] Despite marked improvements in solubility, AORFB operation at high concentrations above 1.5 M has rarely been demonstrated. This may be due to the instability of TEMPO derivatives in high-concentration environments and sharp decreases in electrolyte conductivity.

Herein, we demonstrate the remarkable chemical stabilities of carefully designed TEMPO derivatives compared to those of 4-OH-TEMPO, and revealed that the 'hydroxide-philic' functional group significantly suppressed OH^- access to $R_2N{=}O^+$ in the charged state by UV-vis, electroanalysis, ^{1}H-NMR, and GC-MS spectroscopy. High molecular stability was also confirmed in the charge–discharge performance, with an ultralow capacity decay rate of 0.012% per cycle for over 1000 cycles. *Ex situ* chemical analysis of TEMPO derivatives after long-term cycling clarified the stabilizing effect of this 'hydroxide-philic' functional group. Furthermore, based on their improved solubility, our AORFBs (57.1 Ah L^{-1}) demonstrate the highest volumetric capacity reported to date.

Results and discussion

Decay mechanism of 4-OH-TEMPO

Many previous articles have noticed the sequential contributions of OH^- and H^+ to the degradation of $4\text{-OH-TEMPO}^{\bullet}$ (Scheme 1, route I). OH^- triggers the degradation process by reacting with 4-OH-TEMPO^+ and making the solution acidic. Sequentially, H^+ attacks $4\text{-OH-TEMPO}^{\bullet}$, producing a redox inactive species, 4-OH-TEMPOH. According to this suggested mechanism, OH^- serves only as an initiator, inducing local formation of H^+ around $4\text{-OH-TEMPO}^{\bullet}$; however, the generated H^+ is directly involved in the degradation reaction.[28,29] Besides the proposed decay routes described above, it may also be possible for OH^- to directly react with $4\text{-OH-TEMPO}^{\bullet}$ and/or 4-OH-TEMPO^+ to induce additional decay processes. To obtain

insight into the decay processes, 4-OH-TEMPO$^{\bullet}$ and 4-OH-TEMPO^{+} were treated with neutral, acidic, and basic solutions and their mixtures were analyzed with UV-vis, NMR, and mass spectroscopy.

As the state-of-charge (SoC) of TEMPO-based catholytes increases during charging, the nitroxyl radical (R_2N–$O^{\bullet}$) oxidizes to the oxoammonium cation ($R_2N{=}O^{+}$). The catholyte is thus cycled in a mixture of nitroxyl radicals and oxoammonium cations; their concentration ratio depends on the SoC. To determine which of the two compounds is the main contributor to the degradation of 4-OH-TEMPO, we evaluated the quantitative degradation rates in SoC-0% (*i.e.*, 4-OH-TEMPO$^{\bullet}$) and SoC-100% (*i.e.*, 4-OH-TEMPO^{+}) solutions with an initial formal concentration of 0.1 M. To prepare the SoC-100% solution, 0.5 M 4-OH-TEMPO and 1.0 M NaCl electrolyte was combined with an excess amount of bis(3-trimethylammonio)propyl viologen (BTMAP-Vi) as the anolyte; the mixture was charged fully to SoC-100% and diluted 5 times with D.I. water. Concentration variations of 4-OH-TEMPO$^{\bullet}$ and 4-OH-TEMPO^{+} in both solutions were monitored as a function of time by UV-vis absorption spectroscopy (Fig. 1a and S1, ESI†). The absorption peaks at 429 nm and 476 nm can be assigned to 4-OH-TEMPO$^{\bullet}$ and 4-OH-TEMPO^{+}, respectively.[29] Individual calibration curves for each peak are given in Fig. S2, ESI.† The degradation rate of 4-OH-TEMPO^{+} was even higher than that of 4-OH-TEMPO$^{\bullet}$, indicating that the oxoammonium cation is significantly more responsible for the degradation.

To determine the pH conditions that can provoke degradation, the SoC-0% and SoC-100% solutions were exposed to different acid and base environments for 2 hours after their preparation and the amounts of residual active species were compared by UV-vis analysis. For 4-OH-TEMPO$^{\bullet}$, the nitroxyl radical was fairly stable under both acidic conditions with 0.04 M HCl and basic conditions with 0.04 M NaOH (Fig. 1b and S3, ESI†). That is, the initial concentration of 4-OH-TEMPO$^{\bullet}$ remained almost constant at 0.1 M, irrespective of added amounts of HCl or NaOH. On the other hand, the oxoammonium cation of 4-OH-TEMPO^{+} was notably destabilized after addition of a small amount of NaOH (Fig. 1c and S3, ESI†). The degradation accelerated with increasing amounts of NaOH. For example, after adding 0.04 M NaOH, the active oxoammonium cation degraded to 58.2% of its initial concentration after only 2 hours.

The effects of added H^{+} and OH^{-} on the degradation of 4-OH-TEMPO$^{\bullet}$ and 4-OH-TEMPO^{+} were further investigated by NMR and mass spectroscopy. The structural changes of 4-OH-TEMPO$^{\bullet}$ and 4-OH-TEMPO^{+} were analyzed 2 hours after the solutions had been treated with different amounts of HCl and NaOH. Throughout the experiments, no significant changes were found in the case of 4-OH-TEMPO$^{\bullet}$, as shown in Fig. S4 and S5, ESI.† However, several new peaks appeared in the ^{1}H-NMR and GC spectra of 4-OH-TEMPO^{+} and peak intensity increased with the increase of the amount of NaOH (Fig. S6–S8, ESI†). Particularly, the peaks marked (b) in the ^{1}H-NMR and GC-MS spectra were very noticeable; after comparing them with the spectra of commercially available authentic 4-oxo-TEMPO, they were confirmed to originate from 4-oxo-TEMPO (Scheme 1, route II). The peaks marked (a) are assumed to be from ring opened compounds of 4-OH-TEMPO^{+} because peak (a) in the ^{1}H-NMR spectra can be assigned to allylic hydrogens; the mass of peak (a) in the GC-MS (electron ionization) spectra indicates that the ring opened and, subsequently, N=O fragmented off (Scheme 1, route III). The other two peaks (c and d) in the GC-MS spectra, which started to appear after more than 30 mM NaOH had been added, were presumed based on the spectrometry data to be from compounds 4-OH-TEMPOH and 4-oxo-TEMPOH.

From the above experimental results, a possible decomposition pathway of 4-OH-TEMPO is suggested as shown in Scheme 1. The decomposition process begins with the addition reaction of OH^{-} to oxoammonium of 4-OH-TEMPO^{+}. The resulting adduct is then fragmented into 4-OH-TEMPO$^{\bullet}$ and an OH radical. This generated OH radical readily reacts with 4-OH-TEMPO to produce 4-oxo-TEMPO (Scheme 1, route II).[34] The oxoammonium of 4-OH-TEMPO^{+} can also be a good leaving group, and thus OH^{-} can readily remove a β-proton of the oxoammonium group to yield a ring-opened product in an eliminative manner (Scheme 1, route III). Similar ring opening

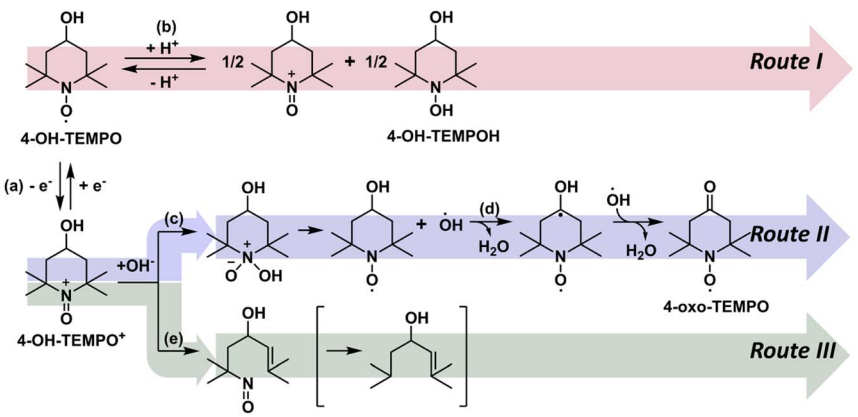

Scheme 1 Possible decomposition pathways of 4-OH-TEMPO: (a) redox reaction between 4-OH-TEMPO and 4-OH-TEMPO^{+}, (b) disproportionation of 4-OH-TEMPO under acidic conditions, (c) reaction of 4-OH-TEMPO^{+} with OH^{-}, (d) reaction of 4-OH-TEMPO with $^{\bullet}$OH *via* the radical pathway, and (e) ring opening reaction by OH^{-} promoted elimination.

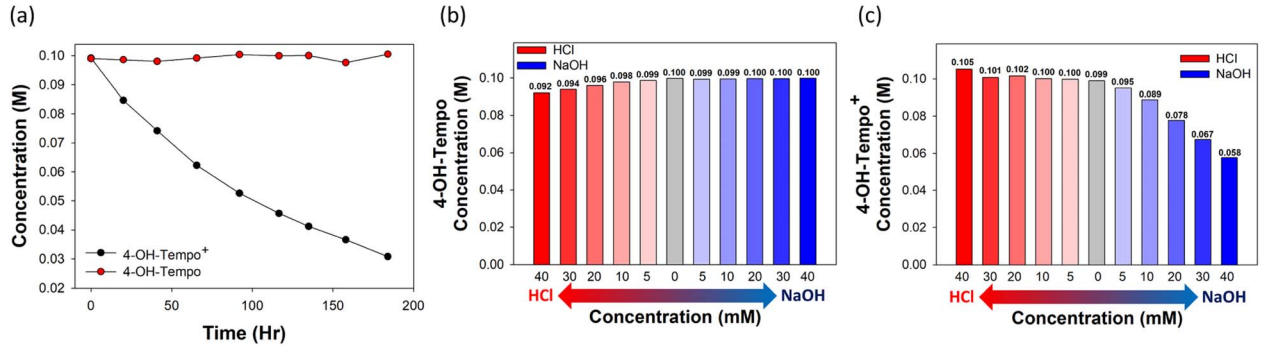

Fig. 1 (a) Concentration variation of 4-OH-TEMPO• and 4-OH-TEMO$^+$ dissolved in 0.2 M NaCl solution under an argon atmosphere at room temperature. The residual concentration of (b) 4-OH-TEMPO• and (c) 4-OH-TEMPO$^+$ 2 hours after treatment with different amounts of HCl or NaOH.

reactions were also reported for 4-carboxylic TEMPO[30] and 4-AcNH-TEMPO.[31] Indeed, after galvanostatic cycling of 4-OH-TEMPO, we observed 4-oxo-TEMPO and a ring-opened compound, as well as 4-OH-TEMPOH (*vide infra*). Here, we have not classified the degradation mechanism by distinguishing between acidic, neutral and basic conditions, because acidic and neutral solutions also contain a small number of OH^- ions. For example, a pH 7 solution contains 10^{-7} M H^+ and 10^{-7} M OH^- ions. Even if a small amount of OH^- is present in the neutral electrolytes, we wanted to pay attention to its accumulated effect on the deterioration of TEMPO during repeated battery operation, *e.g.*, 1000 cycles here.

Molecular design strategy of the decay-resistant TEMPO derivative against OH^- and its rationale based on DFT calculation

After determining that, even at low concentration, OH^- causes the decay of 4-OH-TEMPO, we set up a strategy to synthesize decay-resistant TEMPO derivatives in aqueous solution; it is desirable to modify the structure of TEMPO so that it can sequester OH^- from the redox active functionality of TEMPO. Initially, we conceived a modified TEMPO with a positively charged moiety slightly away from the nitroxyl radical of TEMPO. Thus, the positively charged moiety was able to capture OH^- at some distance from the active site, keeping OH^- ions from reacting with TEMPO. The positively charged moieties were additionally expected to help prevent aggregation of TEMPO molecules, as reported previously.[21] We chose the imidazolium ion as the model positively charged moiety for this study. Furthermore, we envisioned that the imidazolium salts would not only provide TEMPO with a positively charged moiety, but also, because of their ionic character, enhance the solubility of TEMPO in water. To further facilitate the capture of OH^- ions *via* hydrogen bonding, a linker with a carbonyl group, a hydrogen bonding acceptor, was introduced, instead of direct connection of TEMPO with the imidazolium group. Based on these ideas, 4-[2-(*N*-methyl imidazolium) acetoxy]-2,2,6,6-tetramethylpiperidine-1-oxyl chloride (MIMAcO-TEMPO) was designed and synthesized accordingly (Scheme 2). MIMAcO-TEMPO and its intermediate were characterized by ^{1}H-NMR, GC-MS, and HRMS analysis (Fig. S9–S12, ESI†). The synthesized MIMAcO-TEMPO can be considered as an ionic liquid salt. It has been reported that ionic liquids, imidazolium salts, are slightly acidic and the pHs of their aqueous solutions are significantly affected by both substitutions on imidazolium and the counter anions.[35] This is because the cationic moiety would bind with OH^- and/or more complex OH^- containing counter anions, which results in the dissociation of water and production of H^+. In fact, we observed that the aqueous solutions containing 4-[4-(*N*-methylimidazolium)-benzyl-oxyl]-2,2,6,6-tetramethyl piperidine-1-oxyl chloride and 1-butyl-3-methyl imidazolium chloride give almost neutral pH values (6.58 and 6.87, respectively, entries 2 and 4, Table S1, ESI†). When an imidazolium salt is linked with an ester (*i.e.*, 3-(2-methoxy-2-oxoethyl)-1-methyl-1*H*-imidazole-3-ium chloride), it becomes more acidic and more tightly binds with OH^- and/or OH^- containing ions, probably because of the electron-withdrawing nature and hydrogen bonding acceptor capability of the ester functionality. Accordingly, ester-linked imidazolium salts such as MIMAcO-TEMPO and 3-(2-methoxy-2-oxoethyl)-1-methyl-1*H*-imidazole-3-ium chloride give fairly acidic solutions in water (pH 3.19 and 2.81 respectively, entries 3 and 5, Table S1, ESI†). Thus, we assumed that the strong interaction between OH^- and the ester-linked imidazolium of MIMAcO-TEMPO may prevent the attack of OH^- towards the nitroxyl radical of TEMPO.

Density functional theory (DFT) calculations were used to theoretically investigate the affinity of OH^- for 4-OH-TEMPO and MIMAcO-TEMPO in their reduced and oxidized forms. As plausible molecular sites for OH^- attachment, oxygen (site-I) and nitrogen (site-II) of the TEMPO moiety and carbon in the

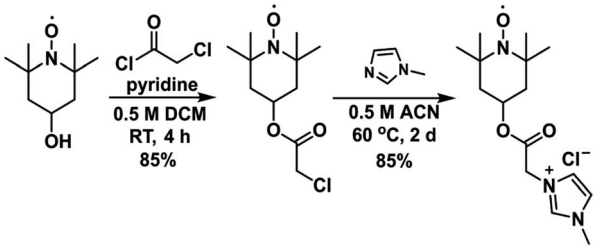

Scheme 2 Synthesis of MIMAcO-TEMPO.

RN^+ = C-NR of the MIMAcO functional group (site-III) were chosen for the calculation of Gibbs free energy changes (ΔG) for each OH^--TEMPO adduct formation; we also investigated the binding affinity of OH^- to various sites of the MIMAcO group (*i.e.* ester linker + imidazolium) of both reduced and oxidized forms of MIMAcO-TEMPO, and found that the interaction between OH^- and site-III in the MIMAcO group had the most negative ΔG. The optimized molecular structures of the OH^--TEMPO adducts after OH^- attachment at each site in the cases of MIMAcO-TEMPO and 4-OH-TEMPO are shown in Fig. S13, ESI. Table S2, ESI,† shows the ΔG of the OH^--TEMPO adduct formation of 4-OH-TEMPO and MIMAcO-TEMPO. In 4-OH-TEMPO, OH^- exhibited a strong binding tendency to site-II of 4-OH-$TEMPO^+$ with a large negative value of ΔG (−0.736 eV), while OH^-showed negligible interaction with the nitroxyl radical of 4-OH-TEMPO. This agreed well with the unstable nature of 4-OH-$TEMPO^+$ in OH^- containing solutions, as confirmed by our experimental results. In MIMAcO-TEMPO, OH^- preferred to interact with site-III of the MIMAcO functional group rather than with the nitroxyl radical or oxoammonium of the TEMPO moiety (site-I or site-II). Therefore, the MIMAcO functional group effectively captured OH^- in the form of the [(OH^- → MIMAcO)-$TEMPO^+$] adduct before OH^- triggered the deactivation mechanism of TEMPO derivatives by combining with oxoammonium.

The strong binding affinity of OH^- with the MIMAcO-functional group significantly affected the electrostatic potential around the TEMPO moiety in the [(OH^- → MIMAcO)-$TEMPO^+$] adduct. Fig. 2 shows optimized molecular structures of MIMAcO-$TEMPO^+$ (singlet) and [(OH^- → MIMAcO)-$TEMPO^+$] adducts (triplet), and their corresponding contour plots of electrostatic potentials. After OH^- was positioned on site-III of the MIMAcO-functional group, the electrons of OH^- were shared in a polarized manner with the oxoammonium cation. This sharing electrostatically prevented the access of OH^- to the oxoammonium cation by changing the electrostatic potential around the oxoammonium cation from electrophilic to nucleophilic. As a consequence, additional OH^--attachment to either site-I or site-II of oxoammonium became non-spontaneous (see Table S2, ESI†).

So far, based on DFT calculations, MIMAcO-$TEMPO^+$ prefers to form the [(OH^- → MIMAcO)-$TEMPO^+$] adduct, in which OH^- binds to the MIMAcO functional group. The $N{=}O^+$ site of the adduct becomes relatively nucleophilic, and OH^- is 'repelled' from the $N{=}O^+$ site. The theoretically estimated OH^--repulsive feature of the [(OH^- → MIMAcO)-$TEMPO^+$] adduct should allow us to anticipate its resilient nature against OH^--driven decomposition during charging and discharging in RFB operation.

Electrochemical characterization of MIMAcO-TEMPO

Fig. 3a shows cyclic voltammograms (CVs) in a solution containing 0.1 M MIMAcO-TEMPO and their best-fit simulation results. MIMAcO-TEMPO shows redox activity with a standard reduction potential of +0.64 V *versus* Ag/AgCl (3 M NaCl), slightly more positive than that of 4-OH-TEMPO (+0.60 V); the CVs of

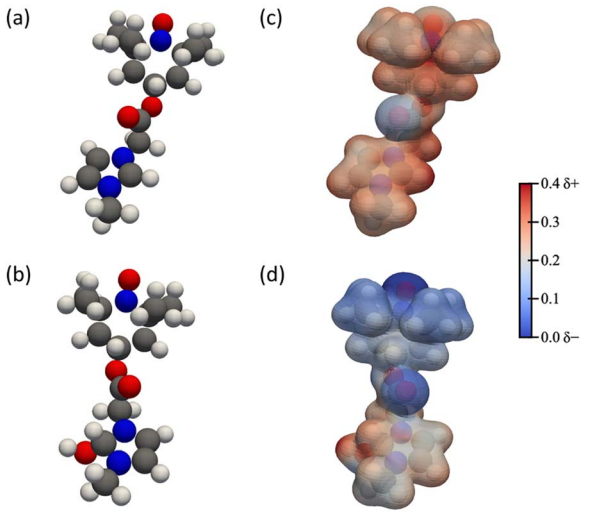

Fig. 2 Optimized molecular structures of (a) MIMAcO-$TEMPO^+$ and (b) [(OH^- → MIMAcO)-$TEMPO^+$], and (c and d) their corresponding contour plots of electrostatic potential, expressed in atomic units (Hartree/*e*).

0.1 M 4-OH-TEMPO with the corresponding best-fit simulation results are also shown in Fig. S14, ESI.† The reactions parameters are listed in Table S3, ESI.† The observed half redox potential shift of MIMAcO-TEMPO to a more positive direction can be explained by the electro-withdrawing effect of the MIMAcO functional group. In the CVs, the cathodic and anodic peak currents can be seen to increase proportionally to the square root of the scan rate ($\nu^{1/2}$), indicating the diffusion-controlled redox reaction of MIMAcO-TEMPO (Fig. S15, ESI†). To analyze the electrochemical kinetic properties, linear sweep voltammetry was conducted on a glassy carbon rotating disk electrode at rotating speeds in a range of 100 to 2500 rpm in 0.5 M NaCl solutions containing either 1 mM MIMAcO-TEMPO (Fig. S16a, ESI†) or the same concentration of 4-OH-TEMPO (Fig. S17a, ESI†). From the linear Levich relationship between the limiting current (j) and the square root of the rotation speed ($\omega^{1/2}$) (Fig. S16b and S17b, ESI†), the diffusion coefficients of both MIMAcO-TEMPO and 4-OH-TEMPO were estimated; the former (6.35×10^{-6} cm^2 s^{-1}) was slightly lower than the latter (8.29×10^{-6} cm^2 s^{-1}), probably because the bulky structure induced by the MIMAcO functional group hindered the mobility of MIMAcO-TEMPO in the electrolyte. From the *y*-intercepts of the Koutecky–Levich plots in Fig. S16c and S17c, ESI,† the kinetic currents (i_k) were obtained at different applied potentials. According to the linear Tafel plot between the log(i_k) and the applied overpotentials (Fig. 3b), the charge-transfer rate constant (k_0) for MIMAcO-TEMPO was estimated to be 1.34×10^{-2} cm s^{-1}, which was nearly twice as high as that of 4-OH-TEMPO (7.11×10^{-3} cm s^{-1}); the estimated values of k_0 for MIMAcO-TEMPO and 4-OH-TEMPO were also in good agreement with the best-fit simulation results shown in Fig. 3a and S14, ESI.† In addition, a higher k_0 of MIMAcO-TEMPO compared to that of 4-OH-TEMPO was identified by electrochemical impedance spectroscopy (EIS); MIMAcO-TEMPO

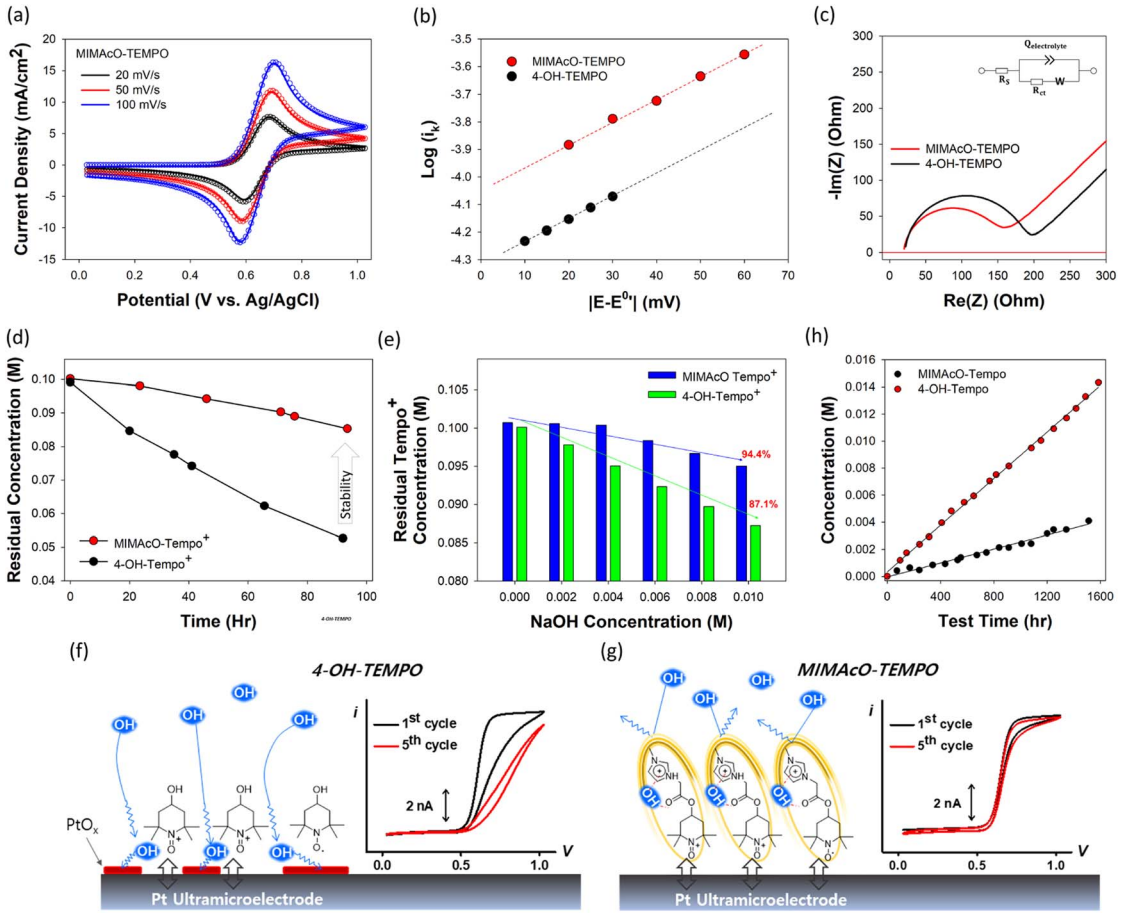

Fig. 3 (a) CVs for the MIMAcO-TEMPO$^{\bullet}$/MIMAcO-TEMPO^{+} redox reaction on a glassy carbon electrode in a 0.1 M MIMAcO-TEMPO + 1.0 M NaCl solution, obtained at scan rates from 0.02 to 0.1 V s^{-1}, (b) Tafel plots between log(i_k) and overpotentials, from which the charge-transfer rate constants (k_0) of the two different types of TEMPO were derived, (c) Nyquist plots obtained by applying an AC voltage of 10 mV amplitude in the frequency range of 100 mHz to 1 MHz at open circuit voltage in solutions containing two different types of TEMPO, (d) concentration variation of MIMAcO-TEMPO^{+} and 4-OH-TEMO^{+} dissolved in 0.2 M NaCl solution under an argon atmosphere at room temperature, (e) residual concentration of MIMAcO-TEMPO^{+} and 4-OH-TEMPO^{+} 2 hours after adding different amounts of NaOH, (f and g) schematics of PtO_x formation and consequently observed voltametric deviations associated with electrode-oxidation of (f) 4-OH-TEMPO and (g) MIMAcO-TEMPO on a Pt ultramicroelectrode where the electrochemical window was from 0.03 to 1.03 V; the aqueous solution contained 0.5 M $NaNO_3$ and pH was adjusted to 6.4, and (h) cross-over concentration of MIMAcO-TEMPO and 4-OH-TEMPO through the AMVN anion exchange membrane as a function of time.

showed smaller charge-transfer resistance (127.6 Ω cm^2) compared to that of 4-OH-TEMPO (165.0 Ω cm^2) (Fig. 3c). Based on the outer-sphere electrode reaction model,[36] the enhanced charge-transfer rate in MIMAcO-TEMPO implies that the reorganization energy of MIMAcO-TEMPO during its electrode oxidation is smaller than that of 4-OH-TEMPO, mainly due to a reduction of solvation energy by the MIMAcO functional group introduced to the TEMPO moiety; this idea is supported by the higher solubility of MIMAcO-TEMPO (*ca.* 3.3 M) compared to that of 4-OH-TEMPO (*ca.* 2.1 M).

MIMAcO-TEMPO^{+} in its fully oxidized state (*i.e.*, in the oxoammonium cation form) exhibited excellent stability over 10 000 cycles without any noticeable voltammetric peak current decrease during the successive voltammetric runs at a scan rate of 100 mV s^{-1} (Fig. S18a, ESI†). In contrast, 4-OH-TEMPO^{+} under the same conditions showed a significant decrease in cathodic peak current, from −9.14 mA cm^{-2} to −7.91 mA cm^{-2}, demonstrating its severe molecular degradation (Fig. S18b, ESI†). The degradation rates of MIMAcO-TEMPO^{+} and 4-OH-TEMPO^{+} at an initial concentration of 0.1 M were quantitatively measured by UV-vis spectrometry and are shown for comparison in Fig. 3d; the corresponding spectra from the MIMAcO-TEMPO^{+} and 4-OH-TEMPO^{+} electrolytes are displayed in Fig. S19, ESI.† The stability of MIMAcO-TEMPO^{+} improved remarkably because the functional group (*i.e.*, MIMAcO–) suppressed the access of OH^{-} ions to the oxoammonium cation, minimizing the irreversible side reactions of TEMPO derivatives; this is consistent with the computational calculation results presented in the previous section.

To investigate the effect of increasing OH^{-} concentration on molecular degradation, different amounts of NaOH were added to the 0.1 M MIMAcO-TEMPO^{+} and 4-OH-TEMPO^{+} solutions and UV-vis spectra were obtained after 2 hours (Fig. S20, ESI†) for the estimation of residual concentrations, which are plotted

in Fig. 3e. With the increases in NaOH concentration, 4-OH-TEMPO$^+$ deteriorated very severely. On the other hand, MIMAcO-TEMPO$^+$ showed high molecular stability with little degradation until the NaOH concentration reached 0.004 M. The residual concentration began to decrease slightly at NaOH concentrations above 0.006 M.

The repelling effect of the functional group on OH^- access to the oxoammonium cation site of MIMAcO-TEMPO was also electrochemically identified through the voltammetric behavior of the two TEMPO derivatives on a Pt ultramicroelectrode (UME), as schematically shown in Fig. 3f and g. At the electrode potential of the TEMPO$^\bullet$/TEMPO$^+$ redox reaction, the Pt surface can be electrochemically oxidized to form multiple layers of platinum oxide (PtO_x), which is coupled with either H_2O or OH^-;[37] the CV on a Pt UME to exhibit the formation of PtO_x and its reduction back to Pt is shown in black line of Fig. S21, ESI.† Therefore, a Pt electrode surface can be concurrently electro-oxidized to highly resistive PtO_x during electro-oxidation of TEMPO$^\bullet$ to TEMPO$^+$.[38] When the cathodic limit in the voltammetric potential window would not be negative enough to drive electro-reduction of PtO_x to Pt in the reverse scan of cyclic voltammetry, electrogenerated PtO_x in the forward scan was not electro-reduced, but remained, which hinders the charge transfer kinetics for electro-oxidation of TEMPO$^\bullet$ in the next voltammetric runs, resulting in a decrease of the corresponding anodic current as the number of voltammetric cycles increases.

For the voltammetric measurements shown in Fig. 3f–g, the bulk pH was adjusted to be 6.4 in both the two cases. In the case of 4-OH-TEMPO, a gradual voltammetric deviation during successive voltammetric runs was observed (see Fig. 3f and S22a, ESI†) mainly due to the accumulation of PtO_x. We experimentally confirmed that the reduction peak potential for PtO_x to Pt at pH = 6.4 was −0.07 V (see Fig. S21, ESI†), and this value is more negative than the cathodic limit of the voltammetric potential window, which is 0.03 V. This result gave rationale for the accumulation of PtO_x in the given voltammetric window. This observation also indicates that a local pH would not be affected by either 4-OH-TEMPO or its electrochemically oxidized form, 4-OH-TEMPO$^+$. In addition, we note that the formation of PtO_x and its accumulation would not be attributed to the liberation of free OH^- by a possible decomposition of 4-OH-TEMPO based on the verification of the voltammetrically distorted behaviour associated with electro-oxidation of $Fe(CN)_6^{4-}$ as shown in Fig. S23, ESI,† from which OH^- cannot be decomposed.

However, in the case of MIMAcO-TEMPO, the successive CV did not show the voltammetric distortion (see Fig. 3g and S22b, ESI†). The observed voltammetric behaviour indicates that electrogenerated PtO_x in the forward scan of the CV would be electro-reduced back to Pt in the reverse in the given voltammetric potential window. This result means that the reduction potential of PtO_x to Pt would be shifted to a more positive value mainly because local pH in the vicinity of a Pt UME would be decreased compared to the bulk one by the electro-oxidation of MIMAcO-TEMPO$^\bullet$; we demonstrate that the reduction potential of PtO_x to Pt is pH-dependent (more specifically local pH dependent),[37,39,40] and the corresponding voltammetric reduction peak was positively shifted as pH decreased as shown in Fig. S21, ESI.†

From the computational calculation results, it is found that OH^- can strongly bind to the MIMAcO functional group of MIMAcO-TEMPO$^+$, not to the oxoammonium site, and be stabilized by the formation of the [(OH$^-$ → MIMAcO)-TEMPO$^+$] adduct. In the adduct, attached OH^- ions affected the electron orbital structure of MIMAcO-TEMPO$^+$, making the oxoammonium site more nucleophilic (*i.e.*, electron-rich) and electrostatically repelling the surrounding OH^- ions. Consequently, local pH on a Pt UME would be decreased, as schematically described in Fig. 3g; for an effectively fast e^- transfer between TEMPO$^\bullet$ and the Pt UME, the electrochemically active nitroxyl radical site of TEMPO$^\bullet$ must be located on the electrode surface at the closest possible distance, while both hydrophilic –OH and MIMAcO– in 4-OH-TEMPO and MIMAcO-TEMPO should be oriented toward the aqueous solution phase for a stabilized interfacial structure at the electrode interface.[41]

Lastly, the transport of TEMPO molecules across the membrane can cause self-discharge, thus decreasing the coulombic efficiency and available capacity of the battery. The permeability of TEMPO derivatives across the anion exchange membrane (Selemion® AMVN) was measured using an H-type cell (Fig. 3h and S24, ESI†). MIMAcO-TEMPO showed a low permeability of 6.10×10^{-10} cm^2 s^{-1}, which is 3.4 times lower than that of 4-OH-TEMPO (2.09×10^{-9} cm^2 s^{-1}). The positive charge of the MIMAcO functional group causes charge repulsion against the ammonium group on the membrane and effectively suppresses the cross-over of MIMAcO-TEMPO. Its bulky structure also contributes to the decrease of cross-over by decreasing the diffusivity in the membrane.

Charge–discharge performance in the AORFB full cell

An AORFB full cell was constructed using 0.1 M MIMAcO-TEMPO and 0.1 M BTMAP-Vi dissolved in 1.0 M NaCl solution as the catholyte and anolyte, respectively (Fig. 4a). A Selemion® AMVN was applied as the anion exchange membrane to permit selective transport of Cl^- anions. To exclude the effect of anolyte-derived capacity loss, an excess volume of BTMAP-Vi anolyte (80 mL) was combined with 40 mL of MIMAcO-TEMPO catholyte. This AORFB cell utilized only one electron charge transfer reaction of BTMAP-Vi, so the cell operated at an open circuit voltage (OCV) of 1.18 V (Fig. 4b). For performance comparison, a reference 4-OH-TEMPO/BTMAP-Vi cell under the same electrolyte conditions was also prepared. Fig. 4c shows a typical charge–discharge curve at a current density of 40 mA cm^{-2}. MIMAcO-TEMPO delivered a discharge capacity of 2.43 Ah L^{-1}, corresponding to 90.7% of the theoretical capacity limit (2.68 Ah L^{-1}). The cell overpotential slightly decreased to 272 mV compared to that of 4-OH-TEMPO (288 mV), due to the improved kinetic effect induced by the MIMAcO functional group. MIMAcO-TEMPO exhibited a notably stable charge–discharge performance, with a coulombic efficiency (CE), voltage efficiency (VE), and energy efficiency (EE) of 99.9%, 79.0%, and 79.0%, respectively.

To investigate the rate capability, the above AORFBs were operated at different current densities from 20 to 100 mA cm^{-2}. The available capacity for MIMAcO-TEMPO was higher than

that for 4-OH-TEMPO for all current densities due to the lower cell overpotential of MIMAcO-TEMPO (Fig. 4d). The difference in the available capacity was more obvious at higher current density. At a current density of 100 mA cm^{-2}, MIMAcO-TEMPO demonstrated a discharge capacity of 1.95 Ah L^{-1} (corresponding to a capacity utilization of 72.8%), while 4-OH-TEMPO had a discharge capacity of 1.79 Ah L^{-1}. Accordingly, depending on the current density, the VE of MIMAcO-TEMPO was slightly higher by 0.8%–2.8% than that of 4-OH-TEMPO (Fig. S25, ESI†). However, it still suffers from poor rate performance compared with flow batteries with some inorganic active species. The low rate performance of these TEMPO derivatives has already been reported in many existing literature studies.[21,30,32,33] Losses in VE can be attributed to various polarization elements such as charge-transfer resistance, mass-transfer resistance, IR-drop of the electrolyte and membrane permeation resistance within the single cell. To investigate the effect of the membrane resistance on the rate performance in more detail, we have compared the charge–discharge behavior in two different anion exchange membranes of Selemion® AMVN and Selemion® DSVN. DSVN is characterized by a lower resistance of 0.8 Ω cm^2 than that of AMVN (2.0 Ω cm^2). The charge–discharge profile at a current density of 40 mA cm^{-2} is shown in Fig. S26a, ESI,† in which the overpotential for DSVN was remarkably reduced compared to that of AMVN. As a result, VE was notably improved from 79.0% to 84.1% (Fig. S26b, ESI†). Therefore, it can be concluded that the membrane resistance played a significant role in lowering VE. For this reason, to improve the rate performance, we plan to focus on developing a low-resistance membrane as future work.

To compare the long-term stability of TEMPO derivatives, the AORFB cells were galvanostatically cycled over 1000 cycles at a current density of 40 mA cm^{-2} (Fig. 4e and S27, ESI†). The average CE of the MIMAcO-TEMPO cell was very high at 99.95%, compared to 99.75% of 4-OH-TEMPO, indicating higher

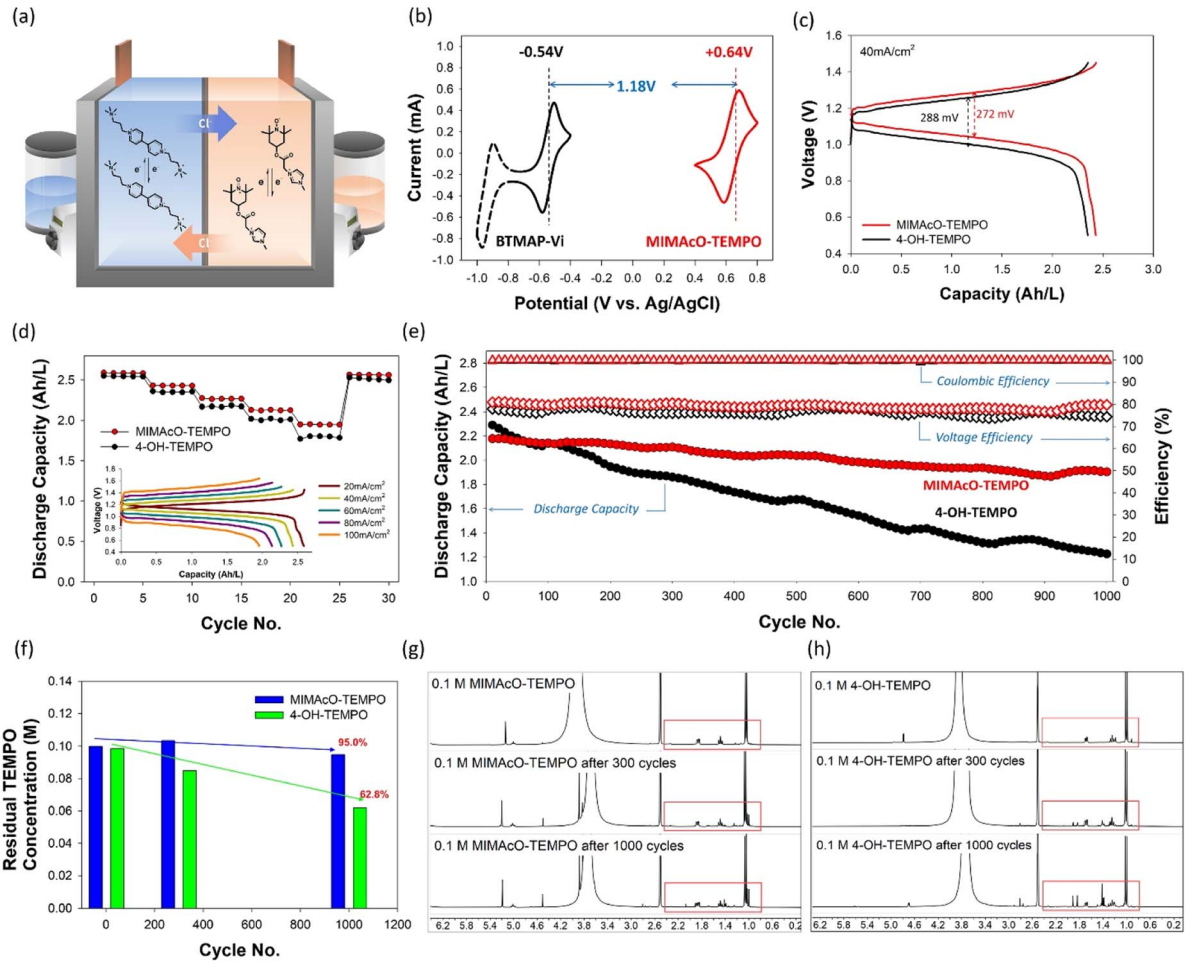

Fig. 4 (a) Structural configuration of MIMAcO-TEMPO/BTMAP-Vi AORFBs. (b) CV curves of 50 mM MIMAcO-TEMPO and BTMAP-Vi in 1.0 M NaCl solution. (c) Galvanostatic charge–discharge profiles of MIMAcO-TEMPO and 4-OH-TEMPO at 40 mA cm^{-2}. (d) Rate capability test as a function of current density (inset: representative charge–discharge profiles of MIMAcO-TEMPO at different current densities). (e) Galvanostatic cycling of MIMAcO-TEMPO and 4-OH-TEMPO at 40 mA cm^{-2} for 1000 cycles. Discharge capacity, CE, and VE were plotted every 10 cycles. (f) Residual concentrations of MIMAcO-TEMPO and 4-OH-TEMPO in the catholyte in the 2nd, 300th, and 1000th cycles during long-term operation. ^{1}H NMR spectra of (g) 0.1 M MIMAcO-TEMPO and (h) 0.1 M 4-OH-TEMPO after the 300th and 1000th cycles recorded in DMSO-d_6. MIMAcO-TEMPO and 4-OH-TEMPO were reduced by phenylhydrazine prior to characterization. AORFBs were tested under 0.1 M MIMAcO/4-OH-TEMPO in 1.0 M NaCl, paired with 0.1 M BTMAP-Vi in 1.0 M NaCl solution.

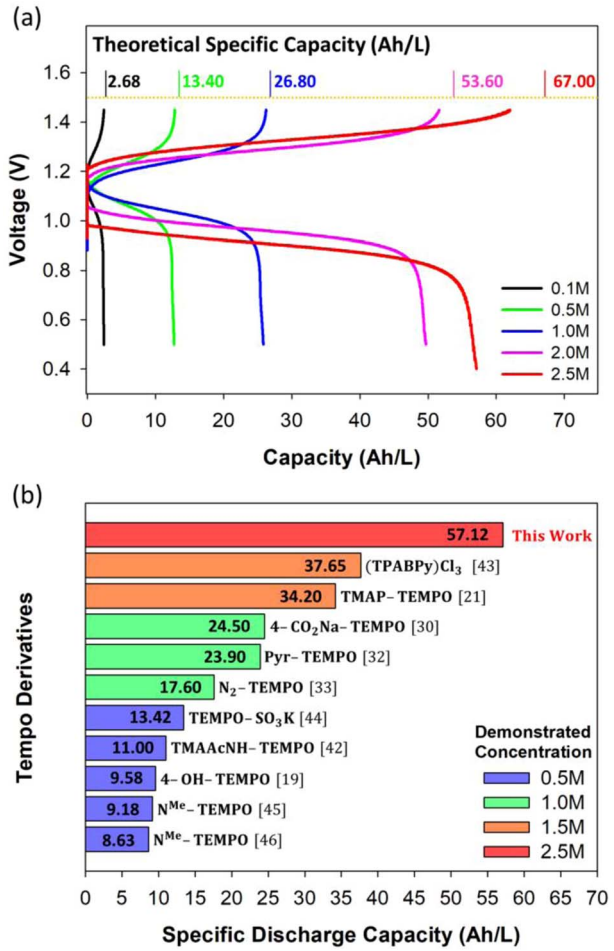

Fig. 5 (a) Charge–discharge curves of the MIMAcO-TEMPO/BTMAP-Vi AORFB at different concentrations of MIMAcO-TEMPO. (b) Specific discharge capacity comparison of AORFBs using various TEMPO-based catholytes from previous studies. Bar colors represent the demonstrated concentrations of TEMPO derivatives in AORFBs.

reversibility in each cycle. Even trivial losses in CE can be accumulated over repeated cycles, resulting in severe capacity decay after prolonged operation. A constant VE of 79.1 ± 1.1% indicated that there was no appreciable deterioration at the interface between the electrolyte and electrode. After 1000 cycles, the MIMAcO-TEMPO cell maintained 88.3% of its initial capacity, corresponding to a capacity decay rate of 0.012% per cycle or a temporal capacity decay rate of 0.078% per h. On the other hand, 4-OH-TEMPO showed sharp capacity loss, with a capacity decay rate of 0.047% per cycle. From comparison to previous studies, MIMAcO-TEMPO can be ranked as one of the most stable TEMPO derivatives (Table S4, ESI†). To analyze the degradation profile after galvanostatic cycling, UV-vis, ^{1}H-NMR, and GC-MS spectrometry studies were conducted. As revealed by the UV-vis spectra, the concentration of MIMAcO-TEMPO active species showed a remarkable retention of 95.0% after 1000 cycles, emphasizing its improved molecular stability (Fig. 4f and S28, ESI†). During the same test period, 4-OH-TEMPO was steadily degraded by 37.2%, from 0.10 M to 0.063 M. The NMR spectra of both 4-OH-TEMPO and MIMAcO-TEMPO after galvanostatic cycling showed decay tendencies similar to those observed from UV-vis spectra (Fig. 4g, h, S29 and S30, ESI†); new peaks with chemical shifts between 0.8 and 2.5 ppm (red box in Fig. 4g and h) were observed during charge–discharge cycling; they were assigned to aliphatic protons of compounds decomposed from 4-OH-TEMPO or MIMAcO-TEMPO, and they are apparently more pronounced for 4-OH-TEMPO than for MIMAcO-TEMPO. GC-MS analysis of 4-OH-TEMPO after 300 and 1000 cycles showed that the same compounds formed as found in the decay mechanism studies above, indicating that 4-OH-TEMPO mainly followed decay routes II and III described in Scheme 1 during galvanostatic cycling (Fig. S31, ESI†). In addition, we performed the cycling test at a higher current density of 100 mA cm^{-2} and found a similar improvement in the decay rate of MIMAcO-TEMPO (Fig. S32, ESI†).

Previous studies have attempted approaches to improve the stability of TEMPO derivatives by substituting the active –OH group with other functional groups. However, as shown in Fig. S33, ESI,† the stability enhancement effect varies greatly depending on the molecular structure of the substituted functional group. When substituting the –OH group with 4-(*N*-methylimidazolium)-benzyl-oxyl group, the obtained TEMPO derivative denoted as TEMPO-1 showed rather poor cycle stability compared to 4-OH-TEMPO.

Another attractive feature of MIMAcO-TEMPO is its high solubility (*ca.* 3.3 M), which is based on the intrinsic hydrophilic properties of the MIMAcO functional group. MIMAcO-TEMPO at different concentrations ranging from 0.1 M to 2.5 M was combined with excess equivalent molar ratios of BTMAP-Vi (detailed concentration information for the anolyte and catholyte is given in Table S5, ESI†). As shown in Fig. 5a, the AORFB was successfully demonstrated with each concentration at a high current density of 40 mA cm^{-2}. As the concentration of MIMAcO-TEMPO increased above 1.0 M, the electrolyte viscosity increased and the ionic conductivity decreased, resulting in a gradual decrease in VE (Fig. S34, ESI†). All the AORFB cells showed a high capacity utilization of more than 85%. Notably, 2.5 M MIMAcO-TEMPO delivered a discharge capacity of 57.1 Ah L^{-1}, the highest volumetric capacity reported to date for AORFBs (Fig. 5b).[19,21,30,32,33,42–46] Although several TEMPO derivatives have been reported to have a high solubility above 3.0 M, none of these have been implemented in AORFBs at concentrations above 1.5 M.[21,32,42] It is also noteworthy that no supporting electrolyte such as NaCl was added to prepare the 2.5 M MIMAcO-TEMPO electrolyte. This is because additional supporting electrolyte can lower the saturation concentration of MIMAcO-TEMPO, causing electrolyte instability. Here, the Cl$^-$ ion, a counter anion constituting MIMAcO-TEMPO, functioned well as a supporting electrolyte. This high concentration AORFB cell showed stable charge–discharge performance with a reasonable VE of 66.6% at a current density of 40 mA cm^{-2}. Furthermore, it achieved a maximum power density of 74.2 mW cm^{-2} at a current density of 130 mA cm^{-2} (Fig. S35, ESI†). This first successful demonstration at a high TEMPO concentration will further increase the practical potential of AORFBs in ESS applications.

Conclusions

Through experimental and computational analysis, we identified OH^- attack on oxoammonium sites in $TEMPO^+$ as the key factor causing TEMPO degradation. Through strategic molecular design of MIMAcO-TEMPO, OH^- was effectively trapped in the intramolecular regime of the hydroxide-philic MIMAcO functional group and the thus generated [$(OH^- \rightarrow$ MIMAcO)-$TEMPO^+$] adduct was characterized as having an OH^- repulsive feature, protecting the oxoammonium site from OH^- attack. This OH^- repelling effect was electrochemically identified *via* voltammetric analysis on the Pt UME. Furthermore, the remarkable degradation mitigation of MIMAcO-TEMPO was confirmed by UV-vis, ^{1}H-NMR, and GC-MS spectrometry studies. Finally, MIMAcO-TEMPO showed a notable improvement in the capacity decay rate to 0.012% per cycle, compared to that of 4-OH-TEMPO (0.047% per cycle), during galvanostatic cycling over 1000 cycles in an AORFB full cell. While a significant portion of 4-OH-TEMPO decomposed into 4-oxo-TEMPO and a ring-opened product during cycling, MIMAcO-TEMPO remained stable, with a retention of 95.0%. Based on the intrinsic hydrophilic properties of the MIMAcO functional group, a high-concentration AORFB with 2.5 M MIMAcO-TEMPO was successfully demonstrated, delivering a discharge capacity of 57.1 Ah L^{-1}. Therefore, the hydroxide-philic and hydro-philic characteristics of the MIMAcO functional group contributed greatly to the improved performance of the TEMPO-based AORFB in terms of both cycling stability and energy density.

Author contributions

Conceptualisation: N. S., K. K., and J. Y., data curation: N. S., K. K., and J. Y., methodology: N. S., K. K., J. Y., S. J. K, H. K., M. S. K., and J. C., investigation: N. S., K. K., J. Y., and S. J. K., visualization: N. S., K. K., J. Y., and S. J. K., supervision: Y. K., Y. S. J., J. C., J. C., and J. H. Y., writing – original draft: all the authors, and writing – revised draft: all the authors. N. S., K. K., and J. Y. contributed equally.

Conflicts of interest

There are no conflicts to declare.

Acknowledgements

This work was supported by the Samsung Research Funding & Incubation Center of Samsung Electronics under Project Number SRFC-MA2101-04.

References

1 G. Li, W. Chen, H. Zhang, Y. Gong, F. Shi, J. Wang, R. Zhang, G. Chen, Y. Jin and T. Wu, *Adv. Energy Mater.*, 2020, **10**, 1902085.
2 W. Lee, G. Park and Y. Kwon, *Chem. Eng. J.*, 2020, **386**, 123985.
3 R. M. Darling, K. G. Gallagher, J. A. Kowalski, S. Ha and F. R. Brushett, *Energy Environ. Sci.*, 2014, **7**, 3459–3477.
4 T. M. Gür, *Energy Environ. Sci.*, 2018, **11**, 2696–2767.
5 W. Huang, X. Feng, X. Han, W. Zhang and F. Jiang, *Cell Rep. Phys. Sci.*, 2021, **2**, 100285.
6 B. S. Min, W. J. Jang, K.-N. Jung, K. B. Kim and J. H. Yang, *Electrochim. Acta*, 2020, **361**, 137075.
7 X. Qian, D.-R. Chang and S. Jung, *Chem. Eng. J.*, 2022, **429**, 132136.
8 J.-H. Lee, R. Kim, S. Kim, J. Heo, H. Kwon, J. H. Yang and H.-T. Kim, *Energy Environ. Sci.*, 2020, **13**, 2839–2848.
9 Z. Li and Y.-C. Lu, *Nat. Energy*, 2021, **6**, 517–528.
10 Y. Yao, J. Lei, Y. Shi, F. Ai and Y.-C. Lu, *Nat. Energy*, 2021, **6**, 582–588.
11 C. Xie, H. Zhang, W. Xu, W. Wang and X. Li, *Angew. Chem.*, 2018, **130**, 11341–11346.
12 B. Yang, L. Hoober-Burkhardt, F. Wang, G. S. Prakash and S. Narayanan, *J. Electrochem. Soc.*, 2014, **161**, A1371.
13 K. Lin, R. Gómez-Bombarelli, E. S. Beh, L. Tong, Q. Chen, A. Valle, A. Aspuru-Guzik, M. J. Aziz and R. G. Gordon, *Nat. Energy*, 2016, **1**, 1–8.
14 Y. Ji, M. A. Goulet, D. A. Pollack, D. G. Kwabi, S. Jin, D. De Porcellinis, E. F. Kerr, R. G. Gordon and M. J. Aziz, *Adv. Energy Mater.*, 2019, **9**, 1900039.
15 S. Jin, Y. Jing, D. G. Kwabi, Y. Ji, L. Tong, D. De Porcellinis, M.-A. Goulet, D. A. Pollack, R. G. Gordon and M. J. Aziz, *ACS Energy Lett.*, 2019, **4**, 1342–1348.
16 D. G. Kwabi, K. Lin, Y. Ji, E. F. Kerr, M.-A. Goulet, D. De Porcellinis, D. P. Tabor, D. A. Pollack, A. Aspuru-Guzik and R. G. Gordon, *Joule*, 2018, **2**, 1894–1906.
17 C. DeBruler, B. Hu, J. Moss, X. Liu, J. Luo, Y. Sun and T. L. Liu, *Chem*, 2017, **3**, 961–978.
18 C. DeBruler, B. Hu, J. Moss, J. Luo and T. L. Liu, *ACS Energy Lett.*, 2018, **3**, 663–668.
19 T. Liu, X. Wei, Z. Nie, V. Sprenkle and W. Wang, *Adv. Energy Mater.*, 2016, **6**, 1501449.
20 R. Feng, X. Zhang, V. Murugesan, A. Hollas, Y. Chen, Y. Shao, E. Walter, N. P. Wellala, L. Yan and K. M. Rosso, *Science*, 2021, **372**, 836–840.
21 Y. Liu, M.-A. Goulet, L. Tong, Y. Liu, Y. Ji, L. Wu, R. G. Gordon, M. J. Aziz, Z. Yang and T. Xu, *Chem*, 2019, **5**, 1861–1870.
22 J. Winsberg, C. Stolze, A. Schwenke, S. Muench, M. D. Hager and U. S. Schubert, *ACS Energy Lett.*, 2017, **2**, 411–416.
23 T. Janoschka, N. Martin, M. D. Hager and U. S. Schubert, *Angew. Chem., Int. Ed.*, 2016, **55**, 14427–14430.
24 B. Hu, C. Seefeldt, C. DeBruler and T. L. Liu, *J. Mater. Chem.*, 2017, **5**, 22137–22145.
25 B. Hu, C. DeBruler, Z. Rhodes and T. L. Liu, *J. Am. Chem. Soc.*, 2017, **139**, 1207–1214.
26 J. E. Nutting, M. Rafiee and S. S. Stahl, *Chem. Rev.*, 2018, **118**, 4834–4885.
27 W. Zhou, W. Liu, M. Qin, Z. Chen, J. Xu, J. Cao and J. Li, *RSC Adv.*, 2020, **10**, 21839–21844.
28 Y. Liu, Q. Chen, X. Zhang, J. Ran, X. Han, Z. Yang and T. Xu, *Curr. Opin. Electrochem.*, 2022, **32**, 100895.

29 A. Orita, M. Verde, M. Sakai and Y. Meng, *J. Power Sources*, 2016, **321**, 126–134.
30 B. Liu, C. W. Tang, H. Jiang, G. Jia and T. Zhao, *ACS Sustainable Chem. Eng.*, 2021, **9**, 6258–6265.
31 H. Fan, B. Hu, H. Li, M. Ravivarma, Y. Feng and J. Song, *Angew. Chem.*, 2022, **134**, e202115908.
32 M. Pan, L. Gao, J. Liang, P. Zhang, S. Lu, Y. Lu, J. Ma and Z. Jin, *Adv. Energy Mater.*, 2022, **12**, 2103478.
33 B. Hu, M. Hu, J. Luo and T. L. Liu, *Adv. Energy Mater.*, 2022, **12**, 2102577.
34 D. L. Marshall, M. L. Christian, G. Gryn'ova, M. L. Coote, P. J. Barker and S. J. Blanksby, *Org. Biomol. Chem.*, 2011, **9**, 4936–4947.
35 X. Cui, S. Zhang, F. Shi, Q. Zhang, X. Ma, L. Lu and Y. Deng, *ChemSusChem*, 2010, **3**, 1043–1047.
36 A. J. Bard, L. R. Faulkner and H. S. White, *Electrochemical Methods: Fundamentals and Applications*, John Wiley & Sons, 2022.
37 P. Daubinger, J. Kieninger, T. Unmüssig and G. A. Urban, *Phys. Chem. Chem. Phys.*, 2014, **16**, 8392–8399.
38 S. Shibata, *Electrochim. Acta*, 1977, **22**, 175–179.
39 D. Pletcher and S. Sotiropoulos, *J. Chem. Soc., Faraday Trans.*, 1994, **90**, 3663–3668.
40 L. W. Liao, M. F. Li, J. Kang, D. Chen, Y.-X. Chen and S. Ye, *J. Electroanal. Chem.*, 2013, **688**, 207–215.
41 E. Mourad, L. Coustan, S. A. Freunberger, A. Mehdi, A. Vioux, F. Favier and O. Fontaine, *Electrochim. Acta*, 2016, **206**, 513–523.
42 H. Fan, W. Wu, M. Ravivarma, H. Li, B. Hu, J. Lei, Y. Feng, X. Sun, J. Song and T. L. Liu, *Adv. Funct. Mater.*, 2022, **32**, 2203032.
43 S. Hu, L. Wang, X. Yuan, Z. Xiang, M. Huang, P. Luo, Y. Liu, Z. Fu and Z. Liang, *Energy Mater. Adv.*, 2021, 2021.
44 X. Junhui, W. Yi, W. Hui, D. Li and L. Chen, *Chem. Lett.*, 2021, **50**, 1301–1303.
45 J. Luo, B. Hu, C. Debruler and T. L. Liu, *Angew. Chem.*, 2018, **130**, 237–241.
46 B. Hu, Y. Tang, J. Luo, G. Grove, Y. Guo and T. L. Liu, *Chem. Commun.*, 2018, **54**, 6871–6874.